Modeling of Vickers Indentation of TiAl Alloys

R. Cagliero and G. Maizza*
Dipartimento di Scienza dei Materiali ed Ingegneria Chimica, Politecnico di Torino
*Corresponding author: C.so Duca degli Abruzzi 24, 10129, Torino, Italy, maizza@polito.it

Abstract:
Instrumented indentation, also known as depth-sensing indentation, is increasingly used as an alternative non-destructive test method to measure mechanical properties of small volumes of materials. It is widely used to determine the hardness equivalent to conventional ones as well as to measure the indentation hardness, the Martens hardness, the indentation modulus, the elastic and plastic parts of the indentation work through the measurement of geometrical quantities such as the contact area. In addition, it permits to estimate the tensile properties. As the force and the displacements are monitored during loading, holding and unloading it also measures the effects of elastic deformation under the indenter.

In this work, the Vickers instrumented indentation test is applied as a non-destructive method to assess the mechanical properties of TiAl samples. These samples are probing disks fabricated simultaneously with real components. An elasto-plastic/contact model is developed to elucidate and interpret the material properties changes during instrumented indentation test. Frictional effects and large deformations are taken into account.

The model is able to predict the loading step of the indentation (F-h) curve as well as the geometry of the contact area, the average contact pressure and the von Mises stress-strain distribution in the sample.

Keywords: Vickers hardness, titanium aluminide, depth sensing indentation, elasto-plastic, contact mechanics, friction.

1. Introduction

In the late 1970s, intermetallic alloys emerged as candidate structural materials for high temperature applications in aerospace and automotive industry as possible replacements for conventional titanium alloys and nickel based superalloys in gas turbine engines [1,2,3,4]. TiAl alloys have excellent mechanical specific properties, creep and oxidation resistance but very low ductility at room temperature.

High resistance alloys, like TiAl alloys, are commonly characterized using high forces and diamond pyramidal indenters, like Vickers indenters. A more advanced indentation test is represented by instrumented indentation, also known as depth-sensing indentation. This test can be conducted under force or displacements control mode.

This study is a preliminary contribution specifically devoted to the development of a suitable computer model. The final purpose is to develop an integral methodology which combines indentation experiments with computer simulations.

In the present work, the instrumented indentation test is carried out on TiAl disks and investigated in combination with finite element predictions. The working disks are probing samples taken from the real production process at specified times. As the microstructure and composition of the disks refer to pre-specified process conditions, the measured indentation properties can be directly related to the mechanical properties of the real components.

The primary purpose in this study is to develop a 3D Vickers instrumented indentation model and to apply it to estimate indentation properties by combining experimental information. These indentation properties will be used to evaluate the mechanical properties of the real components so as the real production process of TiAl components is readily set-up.

The proposed 3D Vickers instrumented indentation model is based on an elasto-plastic stress-strain/contact problem with friction.

To establish a direct relationship between predictions and sample testing a true indentation F-h curve is implemented in the model.

2. Instrumented Indentation

The indentation curve is obtained by high resolution sensors that continuously record the loads and the displacements of the indenter during loading, holding and unloading. Indentation properties can be estimated from the unloading data assuming that the initial unloading is characterized by a pure elastic recovery [9,13,14]. Given an appropriately

fitted experimental unloading curve, the derivative at the maximum depth of penetration is calculated.

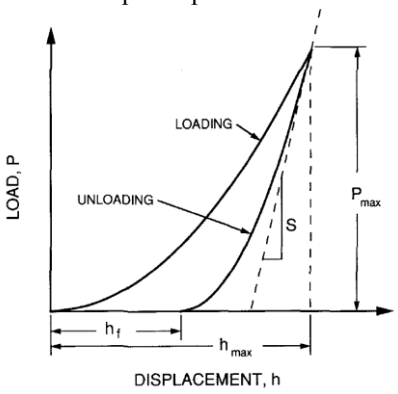

Figure 1. Indentation curve [13].

The so-called contact stiffness S is estimated using the Sneddon's formula [12,13]:

$$S = \left.\frac{dP}{dh}\right|_{h_{\max}} = \frac{2}{\sqrt{\pi}} E^* \cdot \sqrt{A_c} \qquad (1)$$

where $h_{\max}$ is the maximum depth of penetration, A_c is the contact area and E^* is the reduced modulus. The physical meaning of most useful depths of penetration is described in Fig. 2.

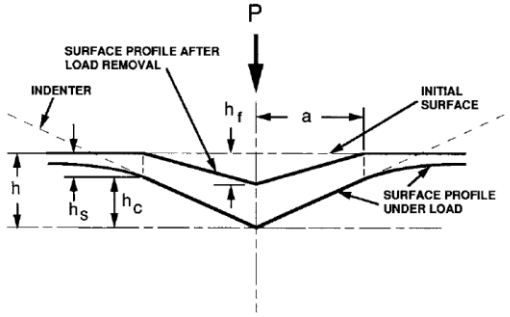

Figure 2. Characteristic depths of penetration.

The reduced modulus, which takes into account the elastic displacements at both the indenter and the sample, can be calculated as:

$$E^* = \left(\frac{1-\nu_0^{\,2}}{E_{IT}} + \frac{1-\nu_{ind}^{\,2}}{E_{ind}} \right)^{-1} \qquad (2)$$

where E_{ind} is the Young's modulus of the indenter, ν_0 and ν_{ind} are the Poisson's ratios of the specimen and of the indenter respectively. For Vickers indenter, the contact area is:

$$A_c = 24.50 h_c^2 \qquad (3)$$

where the contact depth h_c can be estimated as:

$$h_c = h_{\max} - 0.75 \frac{P_{\max}}{S} \qquad (4)$$

The Oliver and Pharr method [13] permits to evaluate the contact area without any optical microscope. The value of this area is influenced by the presence of pile-up or sink-in phenomena (Fig.3).

Figure 3. Sink in and pile-up phenomena [14].

The former is highly correlated with the elasto-plastic behavior of the indented materials.

3 The geometry model

Ideal Vickers indenters are square-based pyramid characterized by an apex angle of 136°. Due to symmetry considerations and experiments the computational domain can be reduced to only a quarter of the whole geometry [12].

Experiments [13] show that real diamond indenters deviate from a perfect geometry due to wear and to the crystallographic structure of diamond. The tip of the modeled indenter is thus truncated at an height of 0.067 mm.

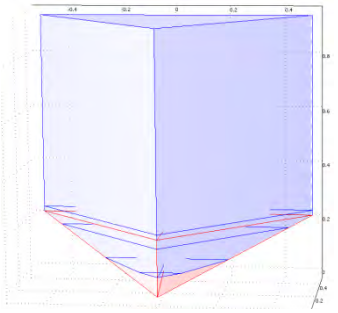

Figure 4. Geometry of the ideal indenter (red) vs modeled indenter (blue).

Thus, an initial triangular contact area between the indenter and the sample of relatively small area (0.005618 mm^2) is assumed. The base of the

indenter is an isosceles triangle with the base angles of 45°, height of 0.733 mm and sides of 3.178 mm and 3.470 mm.

The TiAl sample disks are 2.470 mm in radius and 1.375 mm in thickness.

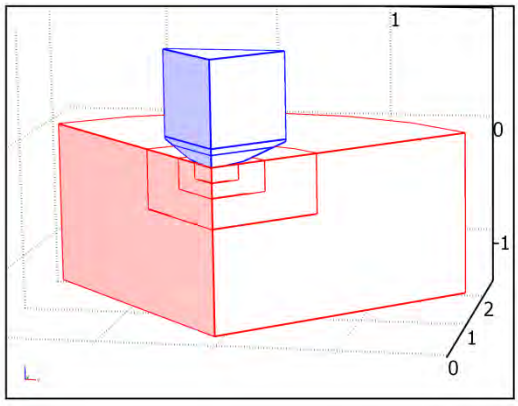

Figure 5. Geometry of the Vickers indentation model.

3.1 The bulk/contact elasto-plastic model

The sample disk is assumed to behave elasto-plastically with isotropic hardening:

$$\sigma_{yhard} = \sigma_{\exp}(\varepsilon_{eff}) - \sigma_y \qquad (5)$$

where σ_y is yield stress and σ_{exp} is an experimental uniaxial true stress-strain tension curve. The value of the total effective strain ε_{eff} in the disk is given by summing the plastic strain ε_{pe} and the elastic strain σ_e/E:

$$\varepsilon_{eff} = \varepsilon_{pe} + \frac{\sigma_e}{E} \qquad (6)$$

where E is the Young's modulus and σ_e is the effective stress that can be computed using the von Mises criterion.

The material of the indenter is assumed to be isotropic.

The 3D Vickers indentation model is implemented in force control mode.

In Comsol Multiphysics 3.5 the contact pair model requires a definition for the master and the slave bodies. The indenter is defined as a master and the disk as a slave. The gap distance g between the slave and the master surface boundaries is preliminarily computed to get the value of both field variables, being the normal contact pressure T_n and the components of the friction traction vector T_t [11]. To ensure a sufficiently constrained indenter over the disk both bodies are assumed to be initially in contact (assembly mode) under a non-zero contact pressure.

3.2 Boundary conditions

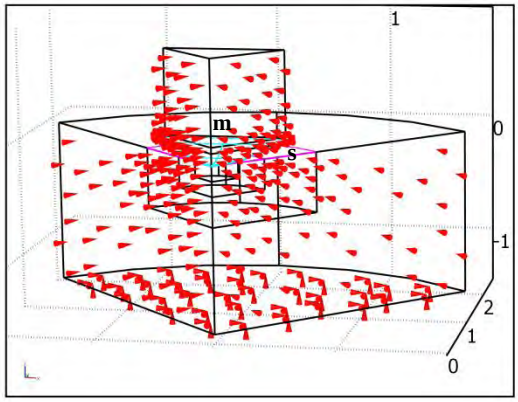

Figure 6. Boundary and contact pair conditions (m = master, s = slave).

In the force control mode the force condition is imposed as distributed load over a surface boundary:

$$\sigma = \frac{F_{load}}{A} \quad \text{loading} \qquad (7)$$

$$\sigma = \frac{F_{\max}}{A} \quad \text{holding} \qquad (8)$$

$$\sigma = \frac{F_{unload}}{A} \quad \text{unloading} \qquad (9)$$

where A is the indenter top boundary area and F_{load} and F_{unload} are defined as:

$$F_{load} = \dot{F} \cdot t \qquad (10)$$

$$F_{unload} = \dot{F} \cdot (t_{tot} - t) \qquad (11)$$

in which t is the time, $\dot{F}$ is the loading rate (i.e. 7,5 N/s) and t_{tot} is the total time of the whole loading history:

$$t_{tot} = t_{load} + t_{hold} + t_{unload} \qquad (12)$$

$F_{\max}$ is set as:

$$F_{\max} = \dot{F} \cdot t_{load} \tag{13}$$

All other boundaries are assumed to be free.

3.3 Domain discretization

To make the 3D Vickers indentation model computationally feasible a relatively *coarse* mesh is selected for both the disk and the indenter as initial *predefined mesh size*. The disk domain is divided into three sub-domains (Fig. 2) to enable different mesh densities to be defined in the slave domain. The maximum element size is set to $5 \cdot 10^{-2}$, 0.13, 0.24 and 0.29 mm for the smaller domain initially involved in the contact, and for the two disk sub-domains respectively. Triangular elements are used throughout. The adaptive mesh option is chosen to identify the regions requiring higher resolution. The error estimator employs the functional norm applied to the global *z* displacement (w). The *rough global minimum* method is selected as *element selection mode* in order to refine the elements with the largest error such that the total number of refined elements is limited to maximum 70% increase. The employed refinement algorithm is the *meshinit* method.

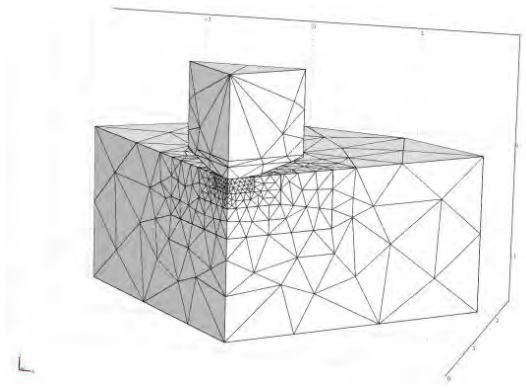

Figure 7. Initial mesh of the indenter-disk system.

3.4 Solution strategy

The Structural Mechanics Module of Comsol Multiphysics 3.5 is employed to work out the 3D elasto-plastic/contact indentation model. As this module does not deal with time dependent contact problems in combination with the elastoplastic solver and friction effect the *parametric segregated* solver [5, 6, 7] has to be used.

This solver splits the overall solution process into two variable groups, i.e. the displacements (first group) and the contact pressure and the components of the friction traction vector (second group). The *parametric segregated* solver uses the *damped Newton method* for each solution step and computes the Jacobian only related to the solution components. This procedure is more effective in terms of memory saving and solution time. The main difference between the standard *parametric* solver and the *parametric segregated* solver is that on failure occurrence the former utilizes the information on the damping factor behaviour whereas the latter considers only the maximum number of segregated iterations and utilizes a factor of 2 to increase the parameter step size, though ignoring the convergence speed of the Newton iteration. The direct UMFPACK is employed to solve the algebraic linear system.

3.5 The contact problem

The contact problem is solved by the *augmented Lagrangian* method [5,6,7,11]. The contact pressure T_n and the friction tractions T_{tx} and T_{ty} are the augmented variables. This method uses the *lumped solver* to minimize possible undershoots in the contact regions. This is set with 25 as maximum iterations number and 1 MPa as tolerance.

An initial very small contact pressure and friction force in z-direction (i.e. 10^{-10} MPa) is required to sufficiently constrain the indenter against the disk. This is functional to prevent solver failures moreover it imparts a very small deformation to the contact pair so as 57 contact points can be detected in the initial loading stage. The *direct search method* detects the subsequent contact points during the loading progress.

Friction effects are considered only in the loading step.

The cohesion sliding resistance, the maximum friction traction and the static friction coefficient are set to 0 MPa, infinite and 0.66 respectively [10].

The tolerances for all *augmented Lagrangian* components are set to 1 MPa. For the *x*, *y* and *z*-displacements, the manual scaling is equal to 0.001.

The *tolerance termination technique* option with a *maximum number of iteration* of 100 is chosen.

The Rayleigh damping parameters, α_{dM} and β_{dK}, are set to 1 s^{-1} and 0.001 s respectively.

4. Experimental data

As the size of the penetration depth is assumed to be much larger than the characteristic grain size of the alloy a bulk behavior is ensured for the disk.

The measured tensile true stress-true strain curve for the TiAl alloy is interpolated by cubic splines (Fig. 8). This is also used to determine σ_{exp} (eq. 5).

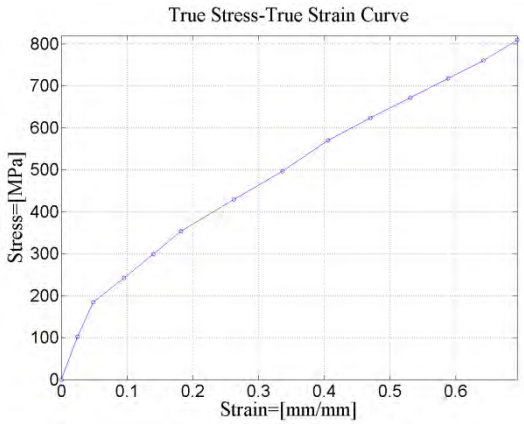

Figure 8. Experimental uniaxial tensile true stress-true strain curve for TiAl alloy.

The Young's modulus and the yield stress of the TiAl alloy are 168 GPa and 275.8 MPa respectively. The Poisson's ratio is 0.263.

The Vickers indenter, made of diamond, has a Young's modulus of 1141 GPa and a Poisson's ratio of 0.100.

The experimental instrumented indentation test on a TiAl alloy disk is realized using an Omag s.a.s prototype indentation device.

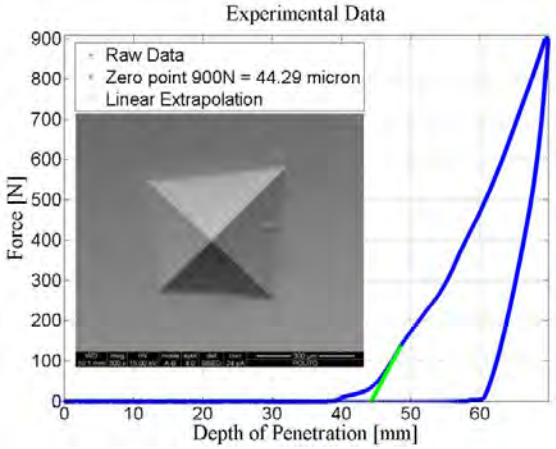

Figure 9. Experimental indentation curve for TiAl sample; the green fitting denotes the linear regression used to detect the zero contact point and real Vickers imprint at Fmax=900 N and loading rate 30 N/s.

The value of the zero point, i.e. the point of initial contact between the real indenter and the sample surface, is evaluated by linear regression (Fig. 9).

5. Results and Discussion

The 3D model is analized for three loading histories, including loading, holding and unloading steps, where each step lasts 1 s, 2.5 s and 5 s (Fig. 10).

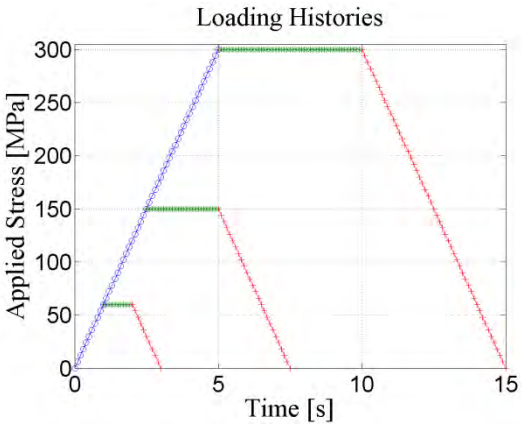

Figure 10. Investigated loading histories.

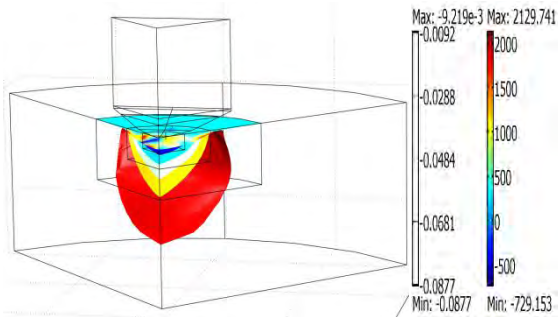

Figure 11. Contact pressure distribution over the slave surface and von Mises iso-stress in the bulk after 5s.

Figure 11 shows the distribution of the contact pressure on the slave surface and the distribution of the von Mises stress in the disk after 5 s. The contact pressure is highly localized at the indenter tip (not very clear in the figure). Similarly, the stress field is highly localized along the periphery of the contact area. It progressively extends over in the bulk of the disk. The maximum stress peak is

reached at the end of the loading time and is equal to 907 MPa.

a)

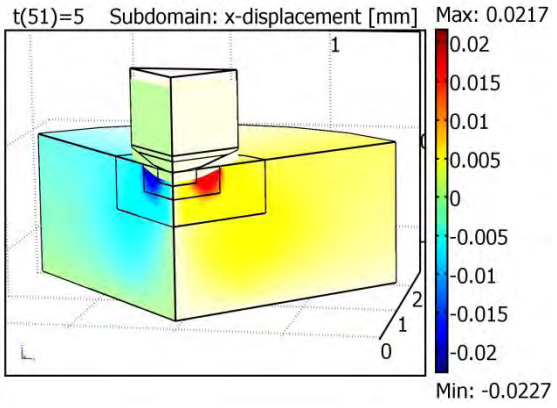

b)

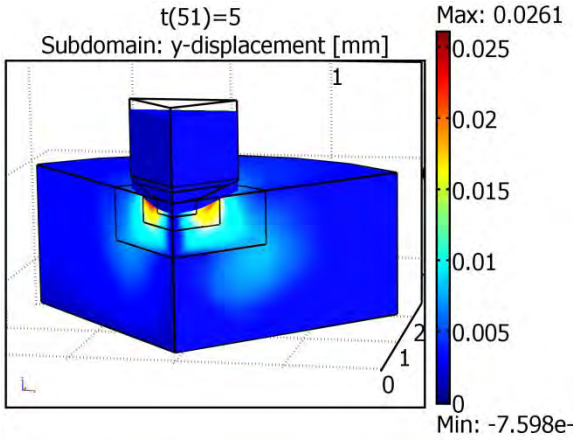

c)

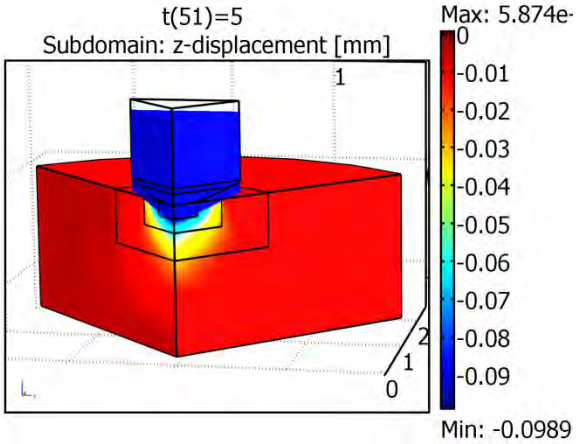

Figure 12. a) x-displacement, b) y-displacement and c) z-displacement maps after 5s.

The x-, y- and z-displacement maps after 5 s are shown in Fig.12. The x- and y- displacements are relatively negligible compared to z-displacements.

However, the maximum values of x- and y-displacements are localized near the contact area periphery. On the other hand, the z-displacements are concentrated under the indenter tip.

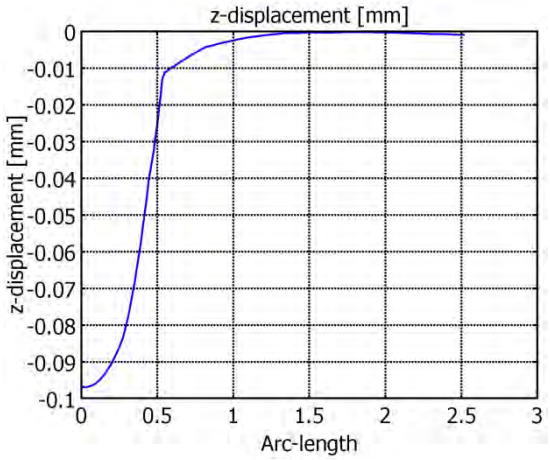

Figure 13. z-displacement of the slave contact surface vs slave boundary arc length after 5 s.

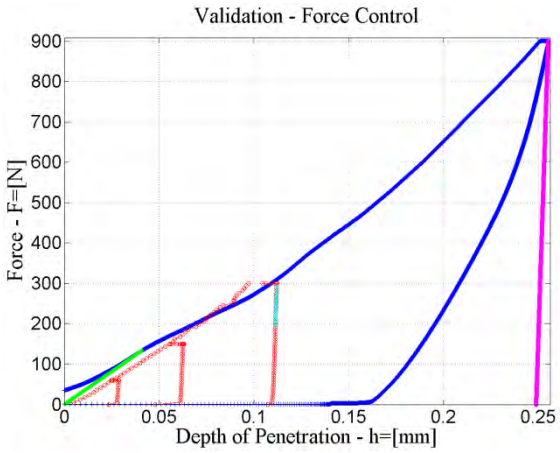

Figure 14. Experimental (blue) and calculated (red) indentation curves. The cyan curve corresponds to the initial 40% of the calculated unloading; the magenta curve corresponds to the derivative at the maximum depth of penetration on the experimental unloading curve. The green curve is used to extrapolate the zero point.

After 5 s, the contact point displaces of 0.0968 mm from the original position. This is appreciated more quantitatively in Fig. 13 for an arch-length=0. From the same figure a slight sink-in is observed over an arch-length (measured along the disk

boundary underneath the indenter on the x-y symmetry plane) of up to 1.5 mm.

Figure 14 compares the experimental and the calculated indentation curves. The experimental curve is the same of that presented in Fig. 9. As already mentioned, the zero point of this curve is found by assuming a linear fitting of the initial 16% of it.

The three calculated indentation curves correspond to the investigated loading histories. They result from the total applied force along the z-direction against the z-displacement of the tip of the indenter. The agreement between the experimental and the calculated curves is good for the three loading steps, as the estimated maximum deviation ($\Delta F/F_{max}$) is equal to (300 - 264.7) / 300 = 0.11. The computed holding steps exhibit small penetration depths with a constant applied force. The three calculated unloading curves, on the other hand, have different curvatures compared to the experimental curve. According to Oliver-Pharr [13], the unloading step is attributed to a purely elastic recovery, although most experiments prove that this step is accompanied by elasto-plastic deformations. Here, the computed unloading step is assumed to be purely elastic. Under this assumption, following the UNI EN ISO 14577-1 standard, we can estimate the contact stiffness taking the 40% of the initial predicted unloading curve. This value is $1.41 \cdot 10^5$ N/mm^2 for the investigated TiAl alloy.

Moreover, the model can estimate the indentation modulus and the indentation hardness.

For the estimation of these two values, Oliver-Pharr [13] suggest the use of the contact depth (h_c in Fig. 2). As an alternative method, we use here a direct computation of the contact area by the help of Fig.15(a). Specifically, from Fig. 15 (a) we read the relative arc-length for a null contact pressure, which corresponds to a semi-diagonal size of 0.5557 mm. Assuming an ideal elastic indenter, given the maximum contact depth of 0.0968 mm, the contact area is estimated as 0.681764 mm^2.

Using eqs. 1 and 2, the indentation modulus and the indentation hardness of TiAl are estimated as high as 160 GPa and 1,3 GPa respectively. These estimations are in good agreement with the experimental values of 176 and 3,9 GPa respectively [15,16].

Note that, the deformed geometry does not indicate the occurrence of a pile-up rather the presence of a sink-in as also observed experimentally (Fig. 9). The depth of the sink-in can be estimated by relating the contact pressure profile of Fig. 15(a) (red curve) and the depth of penetration (blue curve) in the same figure. This size amounts to 0.01106 mm.

a)

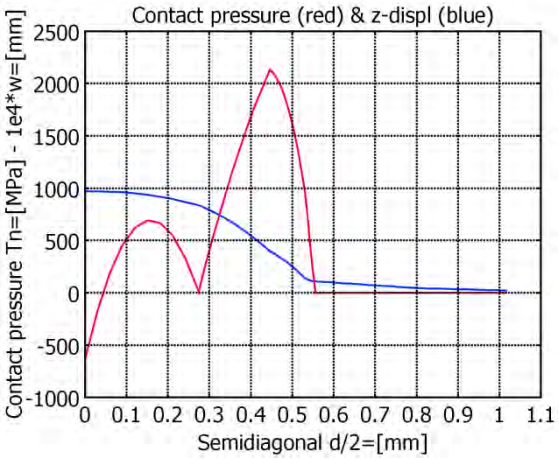

b)

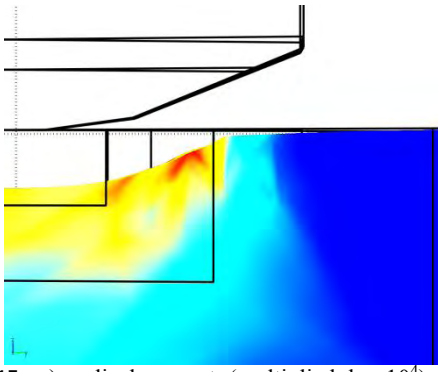

Figure 15. a) z-displacement (multiplied by 10^4) and contact pressure vs slave boundary arc length after 5 s. b) deformed shape and von Mises stress distribution for the same arc length of figure a.

6. Conclusions

A 3D Vickers indentation model has been developed to elucidate the elasto-plastic behaviour of TiAl alloy taking into account friction and large displacements effects. Three loading histories are investigated. The strong geometrical singularity at the indenter tip and to the highly non linear contact mechanics pose severe convergence difficulties. An adequate mesh density at the slave surface is found to be fundamental for both solution convergence and accuracy. The model is successfully validated for the loading indentation step and permits to estimate a number of indentation properties such as

the contact area, the contact stiffness, the indentation hardness and the indentation modulus.

The predicted indentation modulus for TiAl alloy is found to be 160 GPa which is in good agreement with experimental data.

7. References

1. D.M. Dimiduk, Gamma titanium aluminide alloys – an assessment with the competition of aerospace structural materials, *Materials Science and Engineering*, **A263**, 281-288 (1999).
2. X. Wu, Review of alloy and process development of TiAl alloys, *Intermetallics*, **14**, 1114-1122 (2006).
3. Z.H. Huang, Workability and microstructure evolution of Ti–47Al–2Cr–1Nb alloy during isothermal deformation, *Intermetallics,* **13**, 245–250 (2005).
4. M. Thomas, O. Berteaux, F. Popoff, M. Jouiad, G. Hénaff, Microstructure dependence of the strain hardening rate in a PM Ti-48Al-2Cr-2Nb alloy, *3rd International Workshop on γ-TiAl Technologies, Bamberg*, **6**, (2006).
5. Comsol Multiphysics, Structural Mechanics Module, User's Guide, Vers. 3.5 (2008).
6. Comsol Multiphysics, Structural Mechanics Module, Model Library, Vers. 3.5 (2008).
7. Comsol Multiphysics, Structural Mechanics Module, Reference Guide, Vers. 3.5 (2008).
8. A. E. Giannakopoulost, P. L. Larsson, R. Vestergaard, Analysis of Vickers indentation**,** *Int. J. Solids Structures*, **31**, 2679-2708 (1994).
9. K.L. Johnson, Contact Mechanics, *Cambridge University Press*, New York, 4-6, 10 (1985).
10. C.L. Chu, S.K. Wu, A study on the dry uni-directional sliding behaviour of titanium aluminides, *Scripta Metallurgica et Materialia*, **33**, 139-143 (1995).
11. J.C. Simo, T.A. Laursen, An augmented lagrangian treatment of contact problems involving friction, *Computers & Structures*, **42**, 97-116 (1992).
12. T. Niezgoda, J. Malachowski, M. Boniecki, Finite element simulation of Vickers Microindentation on alumina ceramics, *Ceramics International*, **24**, 359-364 (1998).
13. W.C. Oliver, G.M. Pharr, An improved Technique for determining hardness and elastic modulus using load and displacement sensing indentation experiments, *J. Mater. Res.*, **7**, 1564-1583 (1992).
14. J.L.Hay, G.M. Pharr, *Instrumented Indentation Testing*, ASM-handbook-nanoindentation, 1994.
15. J. Xia, H. Dong, T. Bell, Surface properties of a γ-based titanium aluminide at elevated temperatures, *Intermetallics*, **10**, 723–729 (2002).
16. Garima Sharma, R.V. Ramanujan, T.R.G. Kutty, N. Prabhu Indentation creep studies of iron aluminide intermetallic alloy, *Intermetallics*, **13**, 47–53 (2005).

8. Acknowledgements

The authors wish to express their sincere appreciation to Regione Piemonte (local government) – Direzione Regionale alle Attività Produttive - for funding the Green Engine for Air Traffic 2020 (Great 2020 - Ecoprolab) research project of Bando Regionale 24/12/2007 – Misura Ri.7 – Asse 1 "Ricerca e Innovazione" – (LR 34/2004) which has supported the present research work. Also, the AVIO S.P.A. group (Rivalta – TO), AvioProp s.r.l. (NO) and Omag s.a.s (VA) are deeply acknowledged for providing the mechanical data.